Research Article | Vol. 16, No. 11 / 1 Nov 2026 / Optical Materials Express 3946
Optical Materials EXPRESS

Laser-induced damage thresholds of photoresists for high-performance 3D-printed micro-optics in the visible and near-infrared

Sebastian Klein,[1,*] Denys Didychenko,[2] Leander Siegle,[1] Marwan Abdou Ahmed,[2] and Harald Giessen[1]

[1] 4th Physics Institute and Research Center SCoPE, University of Stuttgart, Pfaffenwaldring 57, 70569 Stuttgart, Germany
[2] Institut für Strahlwerkzeuge (IFSW), University of Stuttgart, Pfaffenwaldring 43, 70569 Stuttgart, Germany
[*] sebastian.klein@pi4.uni-stuttgart.de

Abstract: Two-photon polymerization has emerged as a powerful technique for fabricating high-quality micro-optical components for applications such as endoscopy, optical trapping, compact lasers, and micromachining. For many of these uses, the laser-induced damage threshold of the employed photoresists is a key parameter. In this work, we systematically investigate the damage behavior of the commercial two-photon polymerization photoresists IP-S, IPX-S, and IPX-Clear under femtosecond pulsed irradiation at 1040 nm and 520 nm, as well as continuous-wave irradiation at 1030 nm. Damage tests are performed on printed microstructures using automated exposure and optical inspection procedures that enable a comparative assessment of the three materials. We observe clear differences in damage behavior depending on resist type, wavelength, and irradiation regime. Overall, all three photoresists exhibit broadly comparable performance under all tested exposure conditions, with IP-S yielding the highest damage threshold throughout, although in most cases only by a small margin. The damage threshold fluences are in the range of 3 mJ/cm^2 to 140 mJ/cm^2 in pulsed operation and 0.3 MW/cm^2 to 3 MW/cm^2 for continuous-wave irradiation. The results provide practical guidance for selecting two-photon polymerization photoresists for micro-optical components intended for high-power and ultrafast laser applications.

Published by Optica Publishing Group under the terms of the Creative Commons Attribution 4.0 License. Further distribution of this work must maintain attribution to the author(s) and the published article's title, journal citation, and DOI.

1. Introduction

The field of two-photon polymerization (2PP) 3D printing has gained considerable attention in recent years. Improvements in the printing process and optical design using multi-lens free-form optics and the use of gray-scale lithography [1–6] have substantially enhanced optical performance and made these systems viable in many different fields, e.g., optical trapping [7,8], endoscopy [9–14], waveguides [15–19], quantum technology [20–23], and other applications [24–27]. This miniaturization and the rapid development of high-quality free-form optical elements using 2PP, combined with the promising developments in ultrafast material processing with femtosecond pulsed lasers and beam-shaping optics, offer new possibilities for compact micromachining, endoscopy, and laser applications [28–33]. For such applications, a high laser-induced damage threshold (LIDT) of 2PP-printed optics is of great importance. Among the many 2PP photoresists, the damage threshold has already been studied for some materials such as SZ2080, OrmoComp, and IP-S [34–37] with studies focusing on improving the LIDT of resists for use at even higher powers by calcination, improving the resist formulation, or a subsequent coating step [38–40]. In this work, we perform systematic femtosecond pulsed and continuous-wave (cw) LIDT tests on

#614365 https://doi.org/10.1364/OME.614365
Journal © 2026 Received 19 Aug 2026; revised 8 Oct 2026; accepted 13 Oct 2026; published 29 Oct 2026

Optical Materials EXPRESS

three commercial high-quality 2PP photoresists, most of which have not yet been studied, paving the way for high-quality micromachining optics for industrial [41] and medical applications.

2. Experiment

2.1. Setup pulsed tests

To perform damage tests, we use the setup depicted in Fig. 1(a). We use a Stuttgart Instruments Primus laser operating with 7 W at 1040 nm in pulsed femtosecond operation with a repetition rate of 40 MHz. The pulse duration is measured with an APE "Mini" PD DETECTOR NIR autocorrelator and is 0.58 ps. For measurements at 520 nm, the laser is focused into a 4 mm-long LBO crystal for second-harmonic generation (SHG) and collimated again afterwards, also yielding pulse durations <0.6 ps. For power control of our laser, we rotate the polarization direction of our linearly polarized beam with a half-wave plate (HWP) and reflect the unwanted part into a beam block using a polarizing beam splitter (PBS). An electronic shutter (Thorlabs SH05 driven with an SC10 driver, also from Thorlabs) allows us to set exposure times with a few-ms accuracy. The light is focused onto our sample using an aspheric lens (New Focus 5724) with a numerical aperture (NA) of 0.50. An example beam profile in focus (λ = 1040 nm, w = 1.87 µm) is displayed in Fig. 1(b). The spot size is determined by imaging the focal spot

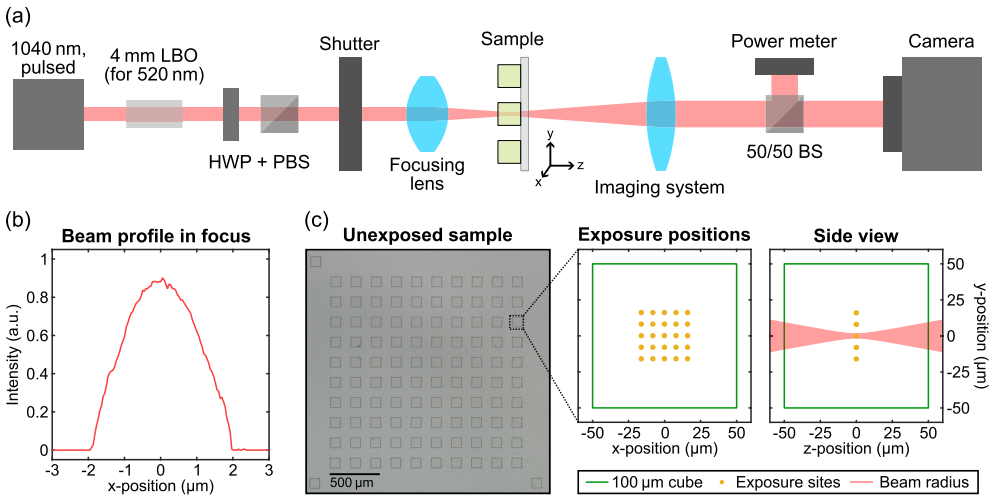


Fig. 1. (a) Measurement setup for exposing photoresist samples with 1040 nm or 520 nm laser light; the latter is achieved by inserting an LBO crystal for SHG. The laser light is focused down onto the sample with a high-NA lens for a sub-2 µm beam waist in focus. Behind the sample, an imaging setup with a camera and a power meter for alignment purposes is used. (b) Measured beam profile in the focal plane. (c) Microscope image of a typical sample before exposure, consisting of a 10 × 10 array of printed photoresist cubes with 100 µm edge length. For the damage tests, the beam focus is placed at 25 different sites in the bulk of the cube, arranged in a planar 5 × 5 array. All sites in each cube are exposed with the same exposure time and power. In the side view, an ideal Gaussian beam envelope is shown using the measured waist of our focus spot.

on a camera (IDS U3-31J0CP Rev.2.2) using a Nikon 60x/0.70 objective and a 200 mm lens. We take multiple images while translating the imaged plane along the optical axis and fit a two-dimensional Gaussian beam profile to each image, determining the smallest beam radius of all images. The beam profile is measured before each experiment after aligning the beam and yields spot sizes between 1.56 µm and 1.65 µm for the 520 nm experiments and 1.87 µm for the

Optical Materials EXPRESS

1040 nm experiments. The differences in spot size at 520 nm arise from small alignment changes between experiments and the insertion of the LBO crystal. Due to the beam profile not being perfectly Gaussian (see Fig. 1(b)), we do not calculate the fluence using the standard formula for a Gaussian beam, but use the captured beam profile image directly for a more accurate result. Using the cumulative sum of all pixel values $\sum_{i,j} I_{ij}$ and the measured average power P of the beam, we determine the power per pixel and count. Dividing this by the square of the pixel size a_{px} divided by the magnification M gives the intensity per count at each pixel. This is multiplied by the maximum pixel value $I_{\max}$ (determined with a 2D Gaussian fit of the top 20 % of the beam profile) and divided by the repetition rate f_{rep} to retrieve the fluence F. The final formula is

$$F = \frac{P \cdot I_{\max}}{\sum_{i,j} I_{ij} \cdot \left(\frac{a_{\mathrm{px}}}{M}\right)^2 \cdot f_{\mathrm{rep}}}. \tag{1}$$

As samples for our damage tests we use the photoresists IP-S, IPX-S, and IPX-Clear by Nanoscribe. These are 2PP photoresists printed in our case with a Nanoscribe QuantumX printer. The chosen sample structure is a 10×10 grid array of cubes with a side length of 100 µm and a distance of 100 µm between the cubes. Additionally, three alignment cubes are printed that are not exposed in our damage tests. These are located outside of the array at three corners to make its orientation unambiguous and are used to precisely locate the sample relative to the focal spot. The exact parameters used for printing our samples are presented in Table S1 of the Supplement 1. After printing, the samples are developed using mr-Dev 600 solution from micro resist technology for a total of about 20 min and placed in isopropyl alcohol (IPA) for another 3 min. The development time is extended if residual liquid resist is still present on the substrate after the first run. After development, the samples are UV-exposed using a Dentmate Prodex N2 UV curing station for 15 min (IP-S and IPX-S) or 2×15 min (IPX-Clear). In Fig. 1(c), an IPX-Clear sample is shown after development and UV-exposure. In the zoom-in, the positions at which each tested cube is exposed are shown. For the damage test exposure on a single cube, the laser is focused into its bulk to significantly reduce the effects of axial misalignment on the measurement results. Each cube is exposed with the same exposure time and power at 25 sites arranged in a 5×5 square grid with a distance of 8 µm between each site. In the side view, we display the exposure positions within a cube, with the calculated Gaussian beam caustic centered on a central exposure site. This caustic is calculated from the measured waist depicted in Fig. 1(b). For accurate LIDT results, the positioning accuracy of the laser spot relative to the exposed cubes/sites is crucial. To achieve a high positioning accuracy and repeatability, we utilize a three-dimensional motorized stage. This stage is automated together with most devices in our setup. This enables the automatic exposure of multiple cubes in sequence and ensures high repeatability of the exposure timing and stage movement. For the alignment, a script semi-automatically locates all three alignment cubes relative to the focal spot and calculates the positions of all cubes in the array. This alignment procedure, which also uses the power meter depicted in Fig. 1(a), is described in detail in Figure S1 of Supplement 1.

In our exposure experiments, typically between 5 and 100 cubes are exposed sequentially by an automated script in which the power and exposure time / pulse number can be varied between cubes. After such an exposure, the sample is inspected under an optical microscope (Nikon Eclipse LV150).

2.2. 1040 nm pulsed tests

In Fig. 2(a), different inspection methods (at 50x magnification) of a cube exposed with our 1040 nm pulsed laser are illustrated. The surface appears unchanged. Moving the focal plane into the cube and thus imaging the bulk where the cube is exposed reveals two exposure sites that are clearly damaged, as well as other sites of the 5×5 grid that exhibit only minute brightness changes. Under dark-field illumination, the two spots reveal strong optical contrast,

Optical Materials EXPRESS

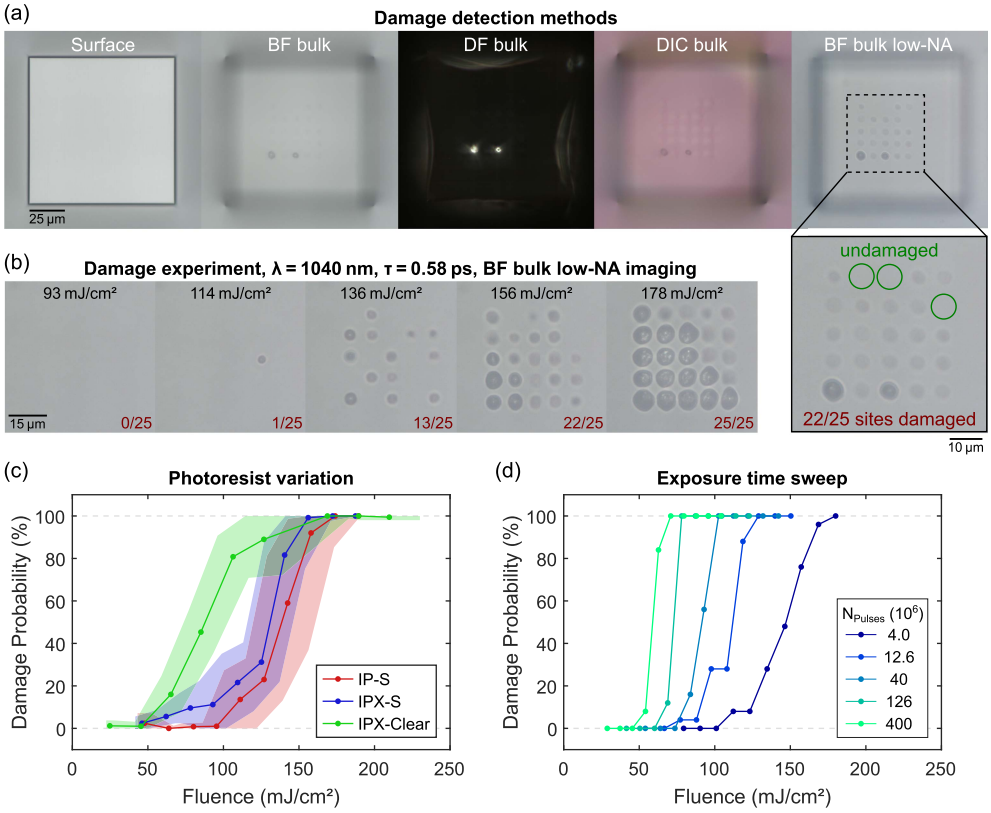


Fig. 2. Damage detection, evaluation, and results for photoresist cubes exposed with 1040 nm pulsed (τ = 0.58 ps) laser light, demonstrated with images of IP-S samples. (a) Comparison of multiple imaging methods of an exposed and partially damaged cube in an optical microscope. Imaging the bulk of the cube in bright-field illumination and closing down the A-stop as much as possible gives the best contrast between damaged and undamaged sites. (b) Low-NA images of cubes exposed with different fluences in a 4×10^6-on-1 test (0.1 s exposure time) and the extracted damage probability. (c) Results for the damage probability over the fluence in focus for three different photoresists irradiated with 4×10^6 pulses and for (d) multiple different pulse numbers for the photoresist IP-S. The light shaded areas represent the combined error from the RMS damage probability and the uncertainty of the fluence measurement.

suggesting that the induced damage has formed a cavity in these two cases. Changes at other sites are not more clearly visible than with bright-field illumination. In differential interference contrast (DIC) imaging mode, the two spots are as visible as in the bright-field case, but the other sites appear more clearly altered by the exposure. The most sensitive imaging method to these small changes is bright-field illumination with the aperture stop (A-stop) closed as much as possible (low-NA imaging). In this way, all the sites that only show small brightness changes in normal bulk imaging now become distinctly noticeable. Furthermore, three sites are identified where even low-NA imaging does not show any laser-induced damage (LID), as illustrated in the zoom-in. Most of the sites seem to have undergone some form of refractive index modification due to the exposure. For the damage evaluation, we count the damaged sites on each cube. We count sites as damaged if they show any kind of modification when viewed with 50x magnification in bright-field bulk low-NA imaging. In our example zoom-in, 22 sites are damaged out of the 25.

Optical Materials EXPRESS

As all sites are exposed in the same way, we use the number of tested sites to apply a statistical approach to the evaluation by calculating the damage probability for each cube. Images of the damaged cubes used for evaluation, ranging from no damage to 100 % damage, are depicted in Fig. 2(b). Here, each site is irradiated with 4×10^6 pulses (0.1 s exposure time). For higher fluences, the damage appears to be more pronounced in the lower left corner of the exposed array. This can be explained by the order in which the sites are exposed. They are exposed starting at the top right site and then proceeding top-to-bottom and right-to-left. This suggests that the damage gradient is a thermal effect, as later-exposed sites experience higher level of damage likely linked to a higher residual temperature inside the cube after the previous site exposures. This is also in line with the top sites being damaged less due to the longer movement delays of the stage moving back to the top, allowing the cube to cool down more. The damage behavior at the damage-onset fluence, on the other hand, is likely not dominated by thermal effects, but rather non-linear processes such as two-photon absorption, as the distribution of damaged sites for lower fluences does not follow the same trend. As can be seen in Figure S2 in Supplement 1, exposing the cubes with a beam size (area) smaller by more than a factor of 2, with the same fluence and therefore much lower power, leads to only a slightly higher damage-threshold curve (factor 1.3). This indicates that the damage behavior is not completely independent of power and associated thermal load, but is predominantly dependent on the fluence. This is consistent with the expectation that nonlinear effects cause the damage at these short pulse durations. As this increase in damage threshold with decreasing spot size could also be attributed to defect- or inhomogeneity-driven damage, caution is advised when comparing damage thresholds as they can not directly be transferred or compared to applications or experiments of significantly different spot sizes.

In this experiment, we exposed 5 cubes per fluence level for the photoresists IP-S and IPX-S, with 10 fluence levels investigated. Due to some cubes detaching from the substrate as a result of the exposure (likely thermal expansion leading to a loss of adhesion), not all cubes could always be used for the probability evaluation. Missing cubes are omitted from the evaluation, reducing the number of cubes over which each value is averaged for some fluences. This occurred almost exclusively with the photoresist IPX-Clear. In anticipation of this problem, in the experiment run on IPX-Clear, 10 cubes were exposed for each fluence level to compensate for the loss of cubes. For the exact number of cubes remaining on the substrate for evaluation, see Figure S3 in Supplement 1.

The result of this experiment is plotted in Fig. 2(c) with the shaded area for each line representing the combined error of the damage-probability root-mean-square (RMS) error and the uncertainty of the fluence value. It proves that IP-S and IPX-S have a very similar damage behavior with a 50 % damage threshold (where on average 50 % of sites are damaged) of around 138(14) mJ/cm^2 and 129(13) mJ/cm^2, respectively, and that IPX-Clear has a lower 50 % damage threshold of around 88(9) mJ/cm^2. IP-S and IPX-S are chemically very similar and thus a similar damage threshold is expected. However, the damage-probability curve of IPX-S is slightly shifted towards lower fluences. This could be due to IPX-S being printed with a lower magnification than IP-S and therefore having a larger internal structure with more inhomogeneity, leading to a slightly increased absorption on average.

In Fig. 2(d), the data of another experiment are shown, where cubes of the photoresist IP-S are exposed with 5 different number of pulses N_{Pulses}. For each pulse count (exposure time), a series of 10 cubes is exposed, where each cube is exposed with a different fluence. The results document that the 50 % damage threshold decreases roughly by a factor of 3 when increasing the pulse count from 4×10^6 to 400×10^6 (exposure times between 0.1 s and 10 s). In another experiment, included in Figure S4 in Supplement 1, the difference in damage between multiple short exposures and a single long exposure at each site is studied. It shows no difference in the damage threshold if the total number of pulses is equal in both cases. In addition to the exposure

Optical Materials EXPRESS

time dependence, the dependence of the damage threshold on different post-treatments (untreated, UV-, and heat-treated) of the photoresist IP-S, inspired by [42], is tested, which resulted in no meaningful change between the treatment methods, as depicted in Figure S5 in Supplement 1.

2.3. 520 nm pulsed tests

In Fig. 3, low-NA microscope images of damaged cubes printed with three different photoresists are displayed after exposure at a wavelength of 520 nm. The images are taken at a 5x magnification with the focus set slightly above the damaged sites. On these cubes, the same experiment approach as for the exposure at 1040 nm is used. To switch to the lower wavelength, an LBO crystal and two lenses are inserted into the beam path for SHG of our pump beam. In Fig. 3(a), the first part of the experiment is shown, displaying the images of 10 cubes of each photoresist after the laser exposure. Each row of 10 cubes is exposed with the same 10 fluence levels with 4×10^6 pulses at each site (as in the experiment at 1040 nm). For all 3 photoresists, the visible damage becomes more severe at higher fluences. This is most pronounced for IPX-S and IPX-Clear, where the cubes start to darken significantly at high fluences, likely due to thermal modification of the resist.

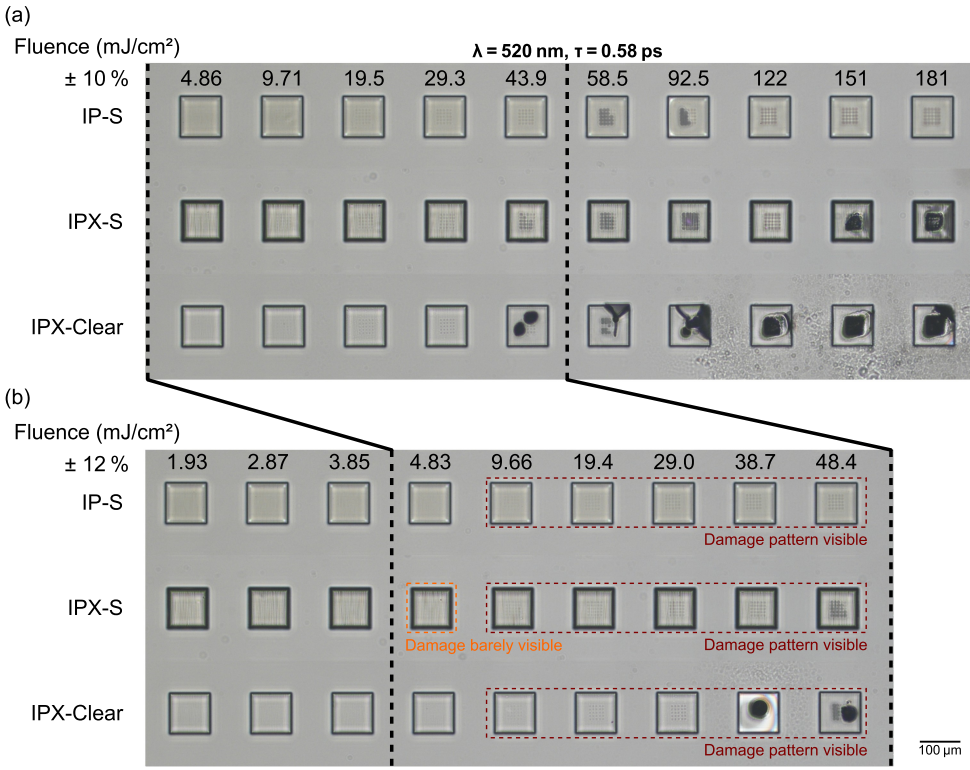


Fig. 3. Microscope images (using the bright-field low-NA imaging mode) of cubes from three different photoresists, exposed at different fluences with 4×10^6 pulses. The exposing laser has a wavelength of 520 nm with a pulse duration of τ = 0.58 ps. The damage visibly increases for higher fluences, although the photoresists exhibit damage in slightly different ways. In (b), cubes from a different exposure with a lower fluence range are presented to better identify the damage threshold. Fluence regions with visible and slightly visible damage are marked in red and orange, respectively.

With IPX-Clear, there is much more surface damage and cracking of the cubes, which starts at around 38.7 mJ/cm^2. We also observe cavities similar to the exposures at 1040 nm (cf. Fig. 2(a)

Optical Materials EXPRESS

and (b)) appearing at medium fluences (around 58.5 mJ/cm^2) for all resists. At lower fluences, all sites on a cube show the same amount of induced changes. As the transition between undamaged and damaged sites is now gradual and the introduced changes are the same for all sites in each cube, the damage-frequency method (as used in Fig. 2) would not improve the evaluation, as there would be no values between 0 % and 100 % of damage probability. We instead revert to a visual approach of determining whether any damage can be identified on a given cube or not. Further insight into choosing this damage evaluation approach due to the different damage morphologies of exposures at 1040 nm and 520 nm can be found in Figure S6 of the Supplement 1.

As we can discern the pattern of damage in the IPX-S row in Fig. 3(a) down to 4.86 mJ/cm^2, we repeat the experiment for all photoresists again but starting at a lower fluence (Fig. 3 (b)). Here, for IP-S and IPX-Clear, the damage pattern starts appearing at around 9.66 mJ/cm^2. Only for IPX-S is a damage pattern also faintly visible at 4.83 mJ/cm^2. We therefore determine the damage threshold for these experiments to be between 4.83 mJ/cm^2 and 9.66 mJ/cm^2 for IP-S and IPX-Clear, and between 3.85 mJ/cm^2 and 4.83 mJ/cm^2 for IPX-S. Reason for this lower damage threshold in comparison to the exposure at 1040 nm might be residual photoinitiator absorption or the change in the order of the absorption process introduced by the lower wavelength. In Figure S7 of the Supplement 1, the results of the 520 nm exposure for different post-treatments of the samples are shown.

2.4. Setup cw tests

In Fig. 4(a), the setup used for cw exposure of the photoresists is depicted, in which we expose our samples to 1030 nm cw laser radiation. The laser used is a TRUMPF TruDisk 8001 with up to 8 kW of available average power. The laser radiation is delivered through an optical fiber with a core diameter of 100 µm and an NA of 0.22. It is coupled into the TRUMPF processing optics, consisting of a collimation unit and a focusing lens, each with a focal length of 200 mm. The laser beam is focused onto the resist sample at an angle of incidence of 10° to avoid back reflection into the laser system. The sample is mounted on a manual three-dimensional stage and can be translated out of the focus to increase the beam size and reduce the corresponding intensity. This position is used as an alternative exposure condition. The beam profile in focus, obtained from the measured caustic, has a diameter of around 105 µm and is displayed in Fig. 4(b). The out-of-focus position is 2 mm away from the focal spot, where the beam diameter is around 300 µm. The final intensity stated for each site is calculated using the respective spot size and the power value after correcting for losses due to interfaces in front of our sample. In Fig. 4(c) on the left, the sample geometry for experiments on this setup is visualized. The printed photoresist structure is a disk of 12.7 mm diameter and 10 µm thickness, printed on a 1 mm thick fused silica substrate. As the printed structure exceeds the maximum printing field size of our printer and the microscope objective used for printing, the structure is split into multiple square printing fields that have a 420 µm (IP-S and IPX-Clear, printed at 25x magnification) or 1100 µm (IPX-S, printed at 10x) side length, with an overlap of the fields of 60 µm and 80 µm, respectively. This results in stitching lines being visible on the sample, especially at low-NA or high-contrast imaging. The post-treatment of these large photoresist disks is similar to the cube samples of our pulsed experiments, with the difference that the disk samples were UV treated and heat-treated at 60 °C for 1 h after development. On the right side in Fig. 4(c), a bright-field microscope image of this sample geometry printed with the photoresist IP-S is shown before any exposure is conducted. Due to the flat and homogeneous sample structure, the alignment is performed manually. Since the minimum output power of the laser was 160 W (corresponding to 1.7 MW/cm^2 at the beam focus), the focus position was first determined without exposing the photoresist sample. For this purpose, a highly reflecting mirror was placed in the beam path before the sample position, and the small leakage transmitted through the mirror was used to measure the caustic with a camera. The determined focus position was marked using two laser pointers crossing at the camera chip,

Optical Materials EXPRESS

and the sample was mounted at their intersection. After mounting the sample, the position was refined by irradiating the sample close to the damage onset and translating it along the z-direction until the strongest modification was observed. This position was used as the focus position for the exposure experiments. The samples are exposed at multiple sites, which are arranged manually in rows by moving the stage after each exposure (Fig. 4(d)). Each exposure is performed for 30 s. Only if severe damage is detected beforehand is the exposure stopped prematurely. The laser power for each exposure, as well as the exposure time, is set beforehand in the laser control software.

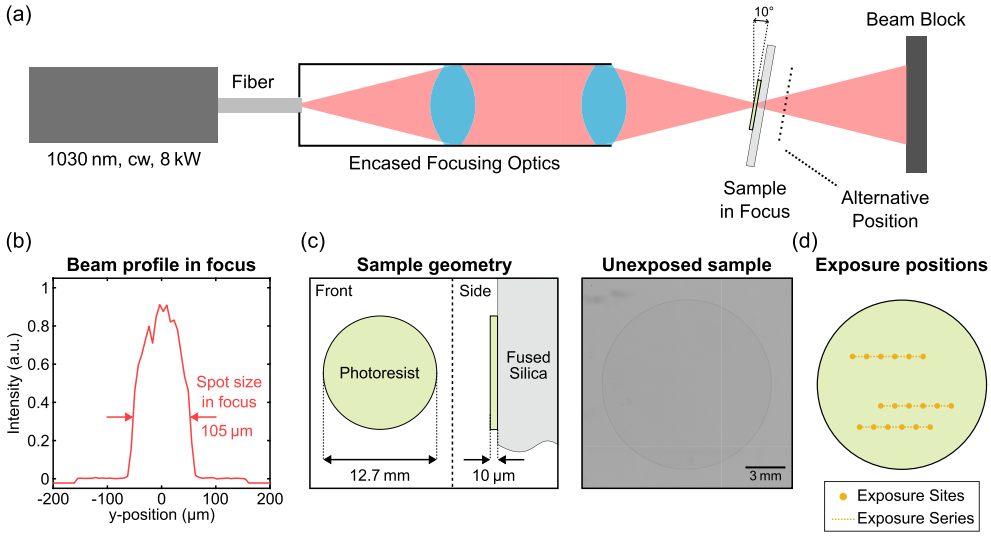


Fig. 4. (a) Schematic of the experimental setup used for LIDT determination at 1030 nm in cw operation. The sample is angled at 10° to prevent back reflections to the source. The alternative position in the beam is used for decreasing the intensity on the sample. (b) Beam profile in the focal point. (c) The sample geometry used in this experiment and a microscope image of an unexposed sample made with the photoresist IP-S. The samples are exposed in rows, where the sites in a row are exposed with increasing laser power from left to right (d).

2.5. 1030 nm cw tests

In this setup, three samples printed with the photoresists IP-S, IPX-S, and IPX-Clear are exposed to 1030 nm cw laser radiation. Microscope images of the samples after the laser exposure are displayed in Fig. 5. The beam diameter is indicated by a red circle for reference, where solid and dashed lines correspond to exposure at the focus and at a 2 mm distance from the focus, respectively. In Fig. 5(a), an overview microscope image of an IP-S sample after exposure with different intensities is shown. Figure 5(b) shows magnified images of selected exposure sites from the same sample. The left and middle images are acquired with an adjusted camera intensity range, restricted to the interval containing the relevant signal. This enhances the contrast and improves the beam footprint and bulk modifications visibility. The right image is shown without additional intensity-range adjustment and is used to visualize the surface modifications under standard microscope display settings. Overall, for this IP-S exposure, the observed modification becomes stronger with increasing intensity. At the lowest tested intensities of 1.72 MW/cm^2 and 2.16 MW/cm^2, only a weak beam footprint is observed, which is mainly visible under adjusted microscope display settings. At intermediate intensities of 2.70 MW/cm^2 and 3.24 MW/cm^2, bulk modifications are observed. Surface modifications start to appear at 3.78 MW/cm^2 and become clearly visible at 4.30 MW/cm^2 and 5.40 MW/cm^2. For the photoresist IPX-S, the exposed sample

Optical Materials EXPRESS

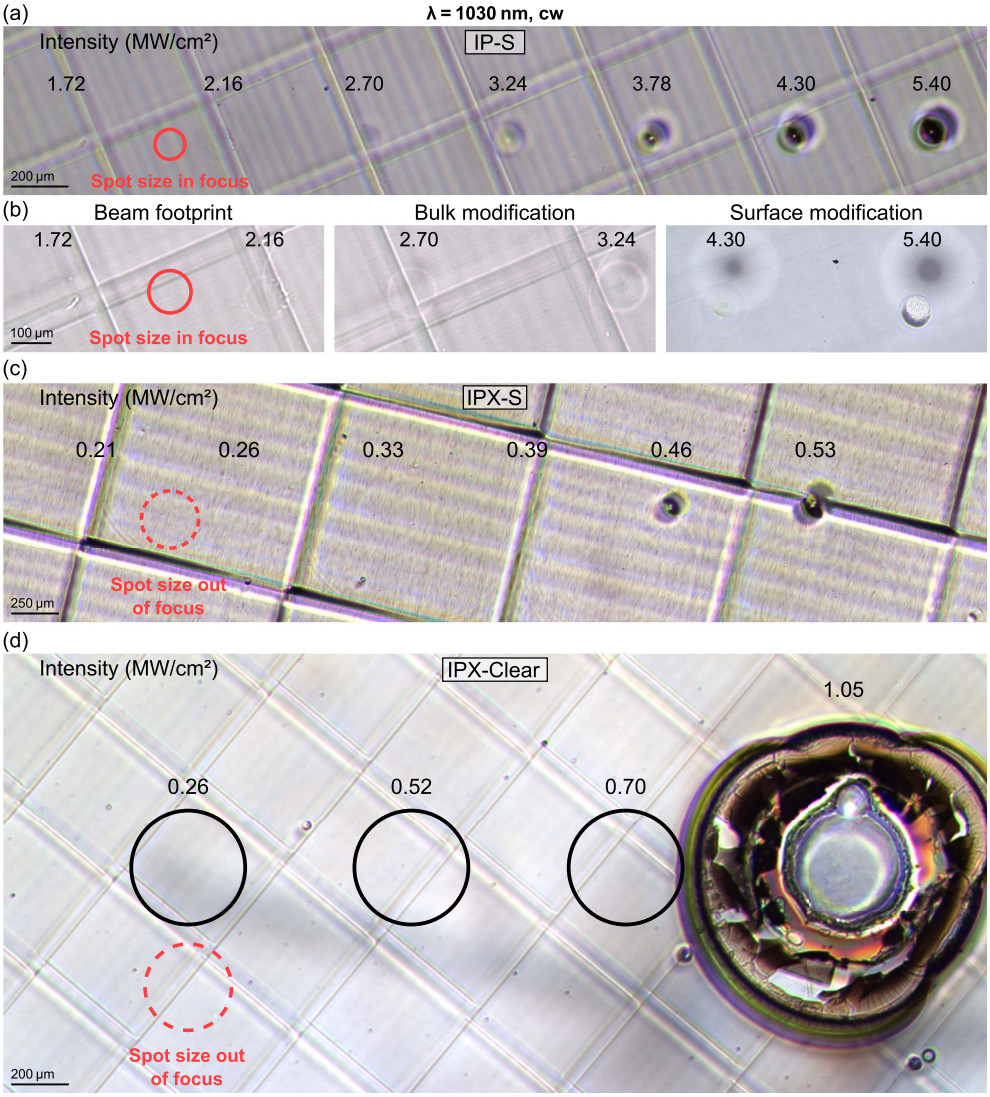


Fig. 5. High-resolution optical microscope images of areas on different photoresist samples exposed at different intensities and spot sizes with a 1030 nm cw laser for 30 s (except most right spot in (d) due to already significant damage after a few seconds). The continuous and dotted circles represent the spot sizes of the spot in focus and out of focus respectively at the different image scales. (a) Exposed IP-S photoresist sample and (b) a contrast-enhanced view of the same exposed sites highlighting the occurring damage morphologies. (c) Exposed IPX-S and (d) IPX-Clear sample. The rectangular lines on the samples are stitching artifacts from the printing process.

is shown in Fig. 5(c). For lower intensities, a weak ring-shaped beam footprint is visible, similar to the low-intensity modification observed for IP-S. No modification beyond the footprint is observed up to 0.39 MW/cm^2, while at 0.46 MW/cm^2, clear damage of the structure appears. For a sample made of IPX-Clear (Fig. 5(d)), exposures up to 0.70 MW/cm^2 lead to no visible changes; however, at an exposure with an intensity of 1.05 MW/cm^2, severe damage of the photoresist is observed. This damage occurred suddenly after around 5 s of the exposure, and the exposure was

Optical Materials EXPRESS

stopped shortly afterwards. The other sites of the IPX-Clear sample are irradiated for the standard exposure time of 30 s, as used for the other sites for this 1030 nm cw experiment. Looking at the results for the three photoresists, we see that the damage onset is roughly of the same order of magnitude for all resists. IP-S withstands the highest intensity, followed by IPX-Clear and IPX-S. Defining the damage threshold as the intensity at which significant damage starts to occur, we obtain a damage threshold for IP-S between 2.16 MW/cm^2 and 2.70 MW/cm^2, for IPX-S between 0.39 MW/cm^2 and 0.46 MW/cm^2, and for IPX-Clear between 0.70 MW/cm^2 and 1.05 MW/cm^2. As the changes in IP-S and IPX-S at the lowest tested intensities are only faintly visible and do not show bulk damage, these are not counted as significant damage. This classification is supported by qualitative camera monitoring of the reflected and transmitted beams, where no pronounced change in the beam appearance was observed for these low-intensity sites. In contrast, at sites with clear damage, the monitored beam image on the beam dump changed visibly during exposure. As the geometry in this experiment could allow for better heat dissipation than what would be expected in free-standing optics, these results may not directly transfer to these applications to the same extent as the experiment performed on thicker photoresist cubes.

3. Conclusion

We studied the damage behavior of the two-photon polymerization photoresists IP-S, IPX-S, and IPX-Clear under illumination with femtosecond-pulsed and continuous-wave laser radiation. For a wavelength of 1040 nm with a pulse duration of 0.58 ps and a repetition rate of 40 MHz, IP-S and IPX-S show similar behavior for the exposure of sub-2 µm-waist positions in the bulk in a 4×10^6-on-1 test (0.1 s exposure time) with damage occurring 50 % of the time at a fluence of 138(14) mJ/cm^2 and 129(13) mJ/cm^2, respectively, and IPX-Clear exhibits a lower 50 % damage threshold of 88(9) mJ/cm^2. For IP-S, this damage threshold decreases by roughly a factor of 3 when increasing the pulse number by a factor of 100. Frequency-doubling the laser and exposing again with 4×10^6 pulses, we find the onset of any visible damage for IP-S and IPX-Clear to be between 4.83 mJ/cm^2 and 9.66 mJ/cm^2, and for IPX-S between 3.85 mJ/cm^2 and 4.83 mJ/cm^2. With a high-power cw laser operating at 1030 nm, the intensity threshold for significant visible damage after laser exposure for 30 s with spot sizes between 105 µm and 300 µm is determined. The threshold is between 2.16 MW/cm^2 and 2.70 MW/cm^2 for IP-S, between 0.39 MW/cm^2 and 0.46 MW/cm^2 for IPX-S, and between 0.70 MW/cm^2 and 1.05 MW/cm^2 for IPX-Clear. With these results, our work provides practical reference values for the design of 2PP-fabricated optical components for compact laser, optical trapping, endoscopic, and micromachining applications operating below the identified damage limits. Future studies could extend this approach to other wavelengths, pulse durations, and application-relevant functional micro-optics, as well as to long-term exposure tests.

Funding. Deutsche Forschungsgemeinschaft (DFG-UP31/1, 431314977/GRK 2642, INST 41/1234-1); Bundesministerium für Forschung, Technologie und Raumfahrt (Integrated3DPrint 13N16874, QLink.X, QR.X, QR.N); Ministerium für Wissenschaft, Forschung und Kunst Baden-Württemberg (Innovation Campus Future Mobility: SdManu1, Lab7, Demo22); Carl Zeiss Foundation (Center QPhoton, EndoPrint3D); European Research Council (3DPRINTEDOPTICS: 862549); European Innovation Council (IV-Lab: 101115545); European Union (MSCA 813159); European Commission (ERDF FEIH_FG_2698214).

Acknowledgment. The authors thank Andy Steinmann for assistance with the SHG setup as well as Serkan Arslan and Dominik Ludescher for fruitful discussions.

Disclosures. The authors declare no conflicts of interest.

Data availability. Data of all damage probability plots of the main manuscript and the Supplement 1 are available in Data File 1, Data File 2, Data File 3, Data File 4 and Data File 5. Data underlying the results presented in other Figures are not publicly available at this time but may be obtained from the authors upon reasonable request.

Supplemental document. See Supplement 1 for supporting content.

Optical Materials EXPRESS

References

1. T. Gissibl, S. Thiele, A. Herkommer, *et al.*, "Two-photon direct laser writing of ultracompact multi-lens objectives," Nat. Photonics **10**(8), 554–560 (2016).
2. S. Thiele, K. Arzenbacher, T. Gissibl, *et al.*, "3d-printed eagle eye: Compound microlens system for foveated imaging," Sci. Adv. **3**(2), e1602655 (2017).
3. M. Schmid, F. Sterl, S. Thiele, *et al.*, "3d printed hybrid refractive/diffractive achromat and apochromat for the visible wavelength range," Opt. Lett. **46**(10), 2485–2488 (2021).
4. L. Siegle, S. Ristok, and H. Giessen, "Complex aspherical singlet and doublet microoptics by grayscale 3d printing," Opt. Express **31**(3), 4179–4189 (2023).
5. S. Wagner, L. Siegle, S. Haeusler, *et al.*, "From two-photon grayscale lithography to scalable replication: Enabling complex aspherical micro-optics for mass production," Adv. Opt. Mater. **13**(30), e02089 (2025).
6. P. Kiefer, V. Hahn, S. Kalt, *et al.*, "A multi-photon (7× 7)-focus 3d laser printer based on a 3d-printed diffractive optical element and a 3d-printed multi-lens array," Light. Adv. Manuf. **4**(1), 28–41 (2024).
7. A. Asadollahbaik, S. Thiele, K. Weber, *et al.*, "Highly efficient dual-fiber optical trapping with 3d printed diffractive fresnel lenses," ACS Photonics **7**(1), 88–97 (2020).
8. C. Liberale, "Micro-3d printed miniaturized systems for optical trapping and manipulation," in *Optical Manipulation and Structured Materials Conference (OMC 2022)*, vol. 12479 (SPIE, 2022), pp. 104–105.
9. T. Gissibl, S. Thiele, A. Herkommer, *et al.*, "Sub-micrometre accurate free-form optics by three-dimensional printing on single-mode fibres," Nat. Commun. **7**(1), 11763 (2016).
10. C. Walker, K. Beckford, T. Tkaczyk, *et al.*, "A 3D-printed reflective lens fabricated via 2-photon polymerization for flexible catheter endoscopy," *Laser 3D Manufacturing XI*, vol. 12876 B. Gu and H. Chen, eds., International Society for Optics and Photonics (SPIE, 2024), p. 128760L.
11. K. Beckford, Y. Ma, J. Liu, *et al.*, "Miniature 3D-printed rod-like refractive objective for endoscopic applications," J. Biomed. Opt. **31**(03), 1–12 (2026).
12. F. Rothermel, A. Toulouse, S. Thiele, *et al.*, "Magnetically actuatable 3d-printed endoscopic microsystems," Commun. Eng. **4**(1), 69 (2025).
13. J. Li, S. Thiele, R. W. Kirk, *et al.*, "3d-printed micro lens-in-lens for in vivo multimodal microendoscopy," Small **18**(17), 2107032 (2022).
14. J. Li, S. Thiele, B. C. Quirk, *et al.*, "Ultrathin monolithic 3d printed optical coherence tomography endoscopy for preclinical and clinical use," Light: Sci. Appl. **9**(1), 124 (2020).
15. G. Berglund, A. Wisniowiecki, J. Gawedzinski, *et al.*, "Additive manufacturing for the development of optical/photonic systems and components," Optica **9**(6), 623–638 (2022).
16. T. Baghdasaryan, K. Vanmol, H. Thienpont, *et al.*, "Design and two-photon direct laser writing of low-loss waveguides, tapers and s-bends," JPhys Photonics **3**(4), 045001 (2021).
17. M. Halendy, S. Ertman, Q. Huang, *et al.*, "Dual-refractive-index photonic crystal waveguides fabricated by combining two-photon polymerization 3d nanoprinting with dose-modified one-photon polymerization," Adv. Opt. Mater. **13**(19), 2500500 (2025).
18. C. R. Ocier, C. A. Richards, D. A. Bacon-Brown, *et al.*, "Direct laser writing of volumetric gradient index lenses and waveguides," Light: Sci. Appl. **9**(1), 196 (2020).
19. P.-I. Dietrich, M. Blaicher, I. Reuter, *et al.*, "In situ 3d nanoprinting of free-form coupling elements for hybrid photonic integration," Nat. Photonics **12**(4), 241–247 (2018).
20. S. Fischbach, A. Schlehahn, A. Thoma, *et al.*, "Single quantum dot with microlens and 3d-printed micro-objective as integrated bright single-photon source," ACS Photonics **4**(6), 1327–1332 (2017).
21. M. Sartison, K. Weber, S. Thiele, *et al.*, "3d printed micro-optics for quantum technology: Optimized coupling of single quantum dot emission into a single mode fiber," arXiv (2020).
22. P. Ruchka, S. Hammer, M. Rockenhäuser, *et al.*, "Microscopic 3d printed optical tweezers for atomic quantum technology," Quantum Sci. Technol. **7**(4), 045011 (2022).
23. S. Mennle, P. Karl, M. Ubl, *et al.*, "Towards fiber-coupled plasmonic perfect absorber superconducting nanowire photodetectors for the near- and mid-infrared," Opt. Continuum **2**(9), 1901–1910 (2023).
24. A. Toulouse, J. Drozella, S. Thiele, *et al.*, "3d-printed miniature spectrometer for the visible range with a 100× 100 μm^2 footprint," Light. Adv. Manuf. **2**(1), 20–30 (2021).
25. M. Deubel, G. Von Freymann, M. Wegener, *et al.*, "Direct laser writing of three-dimensional photonic-crystal templates for telecommunications," Nat. Mater. **3**(7), 444–447 (2004).
26. M. S. Rill, C. Plet, M. Thiel, *et al.*, "Photonic metamaterials by direct laser writing and silver chemical vapour deposition," Nat. Mater. **7**(7), 543–546 (2008).
27. A. Asadollahbaik, A. Kumar, M. Heymann, *et al.*, "Fresnel lens optical fiber tweezers to evaluate the vitality of single algae cells," Opt. Lett. **47**(1), 170–173 (2022).
28. M. Malinauskas, A. Žukauskas, S. Hasegawa, *et al.*, "Ultrafast laser processing of materials: from science to industry," Light: Sci. Appl. **5**(8), e16133 (2016).
29. S. Schmidt, S. Thiele, A. Toulouse, *et al.*, "Tailored micro-optical freeform holograms for integrated complex beam shaping," Optica **7**(10), 1279–1286 (2020).
30. T. Gissibl, M. Schmid, and H. Giessen, "Spatial beam intensity shaping using phase masks on single-mode optical fibers fabricated by femtosecond direct laser writing," Optica **3**(4), 448–451 (2016).

Optical Materials EXPRESS

31. Z. Zhang, L. Siegle, P. Ruchka, *et al.*, "Beam shaping with 3d printed refractive, holographic and diffractive optics on fiber," in *Optica Digital Holography and Three-Dimensional Imaging 2024 (DH)*, (Optica Publishing Group, 2024), p. Tu1A.5.
32. A. Toulouse, M. Wende, T. Kühn, *et al.*, "Towards endoscopic biofabrication: fiber-based two photon lithography," in *3D Printed Optics and Additive Photonic Manufacturing V*, vol. PC14082 A. M. Herkommer, G. von Freymann, and M. Flury, eds., International Society for Optics and Photonics (SPIE, 2026), p. PC140820B.
33. S. Angstenberger, P. Ruchka, M. Hentschel, *et al.*, "Hybrid fiber–solid-state laser with 3d-printed intracavity lenses," Opt. Lett. **48**(24), 6549–6552 (2023).
34. S. Klein, P. Ruchka, T. Klumpp, *et al.*, "Effects of high-power laser radiation on polymers for 3d printing micro-optics," Opt. Mater. Express **13**(12), 3653–3666 (2023).
35. A. Žukauskas, G. Batavičiūtė, M. Ščiuka, *et al.*, "Characterization of photopolymers used in laser 3d micro/nanolithography by means of laser-induced damage threshold (lidt)," Opt. Mater. Express **4**(8), 1601–1616 (2014).
36. A. Butkutė, L. Čekanavičius, G. Rimšelis, *et al.*, "Optical damage thresholds of microstructures made by laser three-dimensional nanolithography," Opt. Lett. **45**(1), 13–16 (2020).
37. L. Jonušauskas, D. Gailevičius, L. Mikoliūnaitė, *et al.*, "Optically clear and resilient free-form μ-optics 3d-printed via ultrafast laser lithography," Materials **10**(1), 12 (2017).
38. D. Gailevicius, R. Zvirblis, K. Galvanauskas, *et al.*, "Calcination-enhanced laser-induced damage threshold of 3d micro-optics made with laser multi-photon lithography," Photonics **10**(5), 597 (2023).
39. E. Kabouraki, V. Melissinaki, A. Yadav, *et al.*, "High laser induced damage threshold photoresists for nano-imprint and 3d multi-photon lithography," Nanophotonics **10**(14), 3759–3768 (2021).
40. D. Astrauskytė, K. Galvanauskas, D. Gailevičius, *et al.*, "Anti-reflective coatings produced via atomic layer deposition for hybrid polymer 3d micro-optics," Nanomaterials **13**(16), 2281 (2023).
41. L. Siegle, M. Wendt, D. Mekle, *et al.*, "3d-printed optics for laser materials processing," Opt. Lett. **51**(16), 4444–4447 (2026).
42. M. Schmid, D. Ludescher, and H. Giessen, "Optical properties of photoresists for femtosecond 3d printing: refractive index, extinction, luminescence-dose dependence, aging, heat treatment and comparison between 1-photon and 2-photon exposure," Opt. Mater. Express **9**(12), 4564–4577 (2019).